RSC Advances

PAPER

View Article Online
View Journal | View Issue

Cite this: *RSC Adv.*, 2025, **15**, 41874

Recycling spent dry cells into rGO/MnO_2 nanocomposites for advanced supercapacitor electrodes

Othai Saha,[ac] Md. Humayun Kabir,*[b] Md. Mazharul Islam,[c] Md. Sanwar Hossain,[a] Muhammad Shahriar Bashar,[d] Md Yeasin Pabel [a] and Sabina Yasmin *[a]

Electronic waste (e-waste) poses a pressing environmental challenge, with improper disposal leading to pollution, resource depletion, and ecosystem damage. In this study, we demonstrate a sustainable strategy to repurpose e-waste into high-performance supercapacitor materials. A reduced graphene oxide/manganese dioxide (rGO/MnO_2) nanocomposite was synthesized entirely from spent dry cells through a cost-effective process. Structural and morphological analyses confirmed a porous nanostructure with a large accessible surface area, enabling efficient charge storage, rapid ion transport, and favorable electrochemical reversibility. Electrochemical testing in 1 M KOH revealed excellent performance, with a specific capacitance of 532 F g^{-1} at 1 A g^{-1}, an energy density of 36.22 Wh kg^{-1} at a power density of 350 W kg^{-1}, and 80% capacitance retention after 1500 cycles. Kinetic analysis indicated a hybrid charge storage mechanism involving both capacitive and diffusion-controlled contributions, with capacitive behavior becoming more dominant at higher scan rates. Impedance measurements further confirmed low charge-transfer resistance and rapid ion diffusion. This sustainable approach for converting e-waste into advanced supercapacitor electrodes demonstrates the potential of hybrid charge storage mechanisms in delivering fast, reversible, and durable energy storage.

Received 9th June 2025
Accepted 21st October 2025

DOI: 10.1039/d5ra04072h

rsc.li/rsc-advances

1 Introduction

Energy plays a vital role in driving scientific, technological, and economic advancements. However, rapid population growth and industrialization have led to a significant rise in global energy consumption. Growing energy demand, environmental pollution, climate change, and fossil fuel depletion underscore the urgent need for efficient, sustainable, and eco-friendly energy storage and conversion technologies, particularly for renewable energy systems.[1,2] In response to these challenges, a broad range of energy devices has been investigated. Energy conversion devices such as photovoltaic cells, thermoelectric devices, and fuel cells are essential for converting solar, thermal, and chemical energy into electricity, thus facilitating the use of renewable resources. However, the irregular output of these energy sources necessitates the implementation of energy storage technologies to ensure a continuous and reliable energy supply.[3–6] Among existing energy storage technologies, batteries and supercapacitors have attracted significant attention. Supercapacitors, in particular, have emerged as an innovative substitute for conventional batteries because of their low internal resistance, excellent charge–discharge rates, high power density, extended cycle stability, and environmental compatibility.[1,2]

Supercapacitors store energy through two fundamental charge storage mechanisms: electrochemical double-layer capacitance (EDLC) and pseudocapacitance. In EDLCs, charge storage is governed by the electrostatic separation of ions in the electrolyte and electrons in the electrode at the interface. While pseudocapacitance stores energy through faradaic (redox) reactions occurring at the electrode surface.[7,8] These devices play a crucial role in high-power applications, including digital devices, emergency doors on airplanes, backup memory systems, electric and hybrid cars, micro-devices, and mobile gadgets. Their performance in such demanding applications largely depends on the characteristics of the electrode materials, such as chemical structure, charge transfer capability, accessible surface area, and structural features. The main electrode materials that are commonly used include graphene-based materials, transition metal oxides, and various conductive polymers.[2,9]

Among transition metal oxides, pseudocapacitive materials have gained considerable interest because of their remarkable

[a]*Institute of National Analytical Research and Service (INARS), Bangladesh Council of Scientific and Industrial Research (BCSIR), Dhanmondi, Dhaka-1205, Bangladesh. E-mail: sabinayasmin@bcsir.gov.bd*

[b]*Institute of Food Science and Technology (IFST), Bangladesh Council of Scientific and Industrial Research (BCSIR), Dhanmondi, Dhaka-1205, Bangladesh. E-mail: humayunkabir@bcsir.gov.bd*

[c]*Department of Chemistry, University of Dhaka, Dhaka-1000, Bangladesh*

[d]*Institute of Energy Research & Development (IERD), Bangladesh Council of Scientific and Industrial Research (BCSIR), Dhanmondi, Dhaka-1205, Bangladesh*

specific capacitance and energy storage capability. Notable examples include NiO, $Ni(OH)_2$, RuO_2, Co_3O_4, MnO_2, and $Co(OH)_2$. In particular, manganese dioxide (MnO_2) is favored due to its excellent pseudocapacitive behavior and high theoretical capacitance.[10,11] However, the effectiveness of MnO_2 is limited due to its low electrical conductivity, low active site density, and particle aggregation during cycling. To overcome these limitations, MnO_2 is often combined with graphene-based support materials. Among them, graphene oxide (GO) and reduced graphene oxide (rGO) are particularly effective due to their high specific surface areas and excellent electrical properties.[12–14] Incorporating MnO_2 with graphene-based materials enhances electrochemical conductivity, increases specific surface area, reduces resistance pathways for ion transport, and prevents particle agglomeration. As a result, MnO_2–graphene composites have attracted significant attention as highly promising candidates for enhancing the electrochemical performance of supercapacitors.[15–17] Recent research on hybrid MnO_2–carbon composites has demonstrated impressive outcomes.[18] For instance, Wenting Xu *et al.* developed an MnO/CNF electrode that exhibited a specific capacitance of 409.7 F g^{-1} at 1 A g^{-1}.[19] Nourali Mohammadi *et al.* synthesized a DMC/MnO_2 nanocomposite, achieving 292 F g^{-1} at 0.5 A g^{-1},[20] while Singhal *et al.* prepared an MnO_2–GO nanocomposite exhibiting a capacitance of 350 F g^{-1} at 0.5 A g^{-1}. These results highlight the immense potential of MnO_2–carbon hybrid materials in supercapacitor technology.[21]

However, these promising results have been achieved using commercial-grade precursors and complex synthesis methods that involve multiple processing steps, high energy consumption, and costly reagents. Such limitations highlight the need for alternative, waste-derived precursors.[22,23] Addressing this challenge, the present study introduces a novel, cost-effective, and environmentally sustainable approach that utilizes spent dry cells as the precursor material for both manganese-based compound and graphite for synthesizing rGO/MnO_2 nanocomposites. Dry cell batteries, commonly used in household electronics, are discarded in large quantities annually, and their improper disposal releases hazardous metals and chemicals into the environment.[23] Notably, these batteries contain MnO_2-rich cathode materials and graphite rods, both of which can be directly converted into functional electrode materials, an opportunity that has been rarely explored in the current literature.[24,25]

Herein, we propose a sustainable and cost-effective strategy to fabricate rGO/MnO_2 nanocomposites by directly reclaiming MnO_2 and graphite from spent dry cell batteries. This approach eliminates the need for costly reagents and energy-intensive processing, offering a scalable pathway consistent with circular economy principles. The recovered graphite is chemically reduced to rGO and integrated with MnO_2 to form a porous, conductive hybrid structure, as confirmed by structural and morphological characterizations. Such architecture is expected to provide a high surface area, efficient electron transport, and shortened ion-diffusion pathways, thereby enhancing both capacitive and diffusion-controlled charge storage. Electrochemical studies further demonstrate that the synergistic interplay between rGO and MnO_2 results in markedly improved specific capacitance, power density, and cycling stability compared to the individual components. By coupling materials recycling with advanced supercapacitor design, this work introduces a novel waste-to-resource route that not only addresses environmental concerns but also delivers mechanistic insights into the favorable charge kinetics governing high-performance energy storage.

2 Experimental

2.1 Reagents and chemicals

Potassium permanganate ($KMnO_4$) and sulfuric acid (H_2SO_4) were obtained from Scharlau, Spain. Phosphoric acid (H_3PO_4) was purchased from Janssen Chemica, Belgium, while oxalic acid ($C_2H_2O_4$) was collected from Scharlau, Spain. Hydrochloric acid (HCl) and sodium hydroxide (NaOH) were obtained from Sigma-Aldrich, USA. Potassium hydroxide (KOH) and hydrazine hydrate ($N_2H_4 \cdot H_2O$) were obtained from AppliChem, Germany. Reagents of high purity were employed in their supplied form, and ultrapure deionized water (18 MΩ cm) served for the preparation of all solutions.

2.2 Instruments

The prepared samples were characterized using multiple analytical techniques. Fourier-transform infrared (FT-IR) spectra were obtained using a Fourier transform spectrophotometer (Frontier FT-NIR/MIR, PerkinElmer, USA) in transmittance mode. X-ray diffraction (XRD) patterns were obtained with an Ultima IV (Rigaku, Japan) using a Cu K_α source (1.5406 Å). Surface morphology was examined using scanning electron microscopy (SEM) (EVO18, Carl Zeiss, AG, Germany), and images were captured at different magnifications with a voltage of 15 kV. Energy-dispersive X-ray spectroscopy (EDX) with a TEAM EDS system (EDAX, USA) was employed to analyze the elemental composition. Transmission electron microscopy (TEM) (JEOL JEM 2100F, Japan) was employed for morphological characterization at an accelerating voltage of 200 kV with field emission capabilities. Electrochemical studies were performed using a CHI660E instrument (USA), employing a glassy carbon (GC) working electrode (CHI104, diameter = 3 mm), a saturated Ag/AgCl/KCl reference electrode (CHI111), and a spiral platinum wire (BAS Inc., 23 cm) as the counter electrode.

2.3 Extraction of graphite powder

Spent dry cells collected from residential and commercial areas were used to extract graphite powder, following our previously reported method.[26,27] Briefly, the graphite rods were retrieved by carefully disassembling the dry cells. Initially, the rods were cleaned with tissue paper and washed with DI water to eliminate surface contaminants, followed by air-drying at room temperature and grinding into fine powder with a mortar and pestle. To ensure complete purification, the resulting powder was subjected to aqua regia treatment and multiple washes with

DI water until neutrality was attained. Finally, the purified graphite was dried overnight at 50 °C.

2.4 Synthesis of GO

GO was synthesized from the obtained graphite powder using the improved Hummer's method as shown in Scheme 1.[28–31] Briefly, a mixture of H_2SO_4 and H_3PO_4 in a 9 : 1 volume ratio (270 mL H_2SO_4 and 30 mL H_3PO_4) was taken in a round-bottom flask. Approximately 2 g of graphite powder was gradually added to the reaction mixture under stirring, followed by the slow addition of 12 g $KMnO_4$. The reaction mixture was heated at 50 °C for 12 hours, then cooled to room temperature. Subsequently, H_2O_2 solution (6 mL, 30%) was carefully added under stirring to decompose the excess $KMnO_4$, with an ice bath used to control the exothermic reaction. The precipitate was collected by centrifugation (5000 rpm, 10 min) and subjected to successive washes with DI water and 30% HCl to eliminate metal impurities. Additional rinses with DI water and ethanol were carried out to eliminate residual chloride ions. Finally, the purified GO was vacuum-dried overnight at 50 °C to obtain the final product. The recovered GO is characterized by SEM and Raman spectroscopy, which is consistent with previous literature (SI Fig. S1).

2.5 Synthesis of $MnSO_4$ from MnO_2

MnO_2 in the form of a black paste was extracted from the cathode material of spent dry cells. The recovered paste was thoroughly washed and filtered to remove soluble contaminants, such as zinc chloride ($ZnCl_2$) and ammonium chloride (NH_4Cl). The purified MnO_2 paste was then gradually introduced, with continuous stirring, into an acidic medium consisting of concentrated sulfuric acid and an aqueous solution of oxalic acid in deionized water. The reaction was continued until gas evolution ceased, indicating the complete conversion of MnO_2 into manganese sulfate ($MnSO_4$).The mixture was subsequently filtered to separate any insoluble residues. The clear filtrate was concentrated by heating at 50 °C, resulting in the precipitation of $MnSO_4$ crystals. The obtained crystals were separated through filtration, thoroughly rinsed with DI water, and subsequently dried overnight at 50 °C. The prepared MnSO4 is characterized by SEM, XRD and FTIR (SI, Fig. S2 and S3).

2.6 Synthesis of rGO/MnO_2 nanocomposite

The rGO/MnO_2 nanocomposite was prepared *via* a simple chemical reduction method. A schematic representation of the preparation process is provided in Scheme 1. Initially, 100 mg of GO and 50 mg of manganese sulfate ($MnSO_4$) were individually dispersed in 100 mL of DI water and subjected to sonication separately for one hour to ensure uniform dispersions. Under constant stirring, the $MnSO_4$ solution was slowly added to the GO suspension, followed by dropwise addition of 1 M NaOH to adjust the pH to 11. Subsequently, hydrazine hydrate was slowly introduced as a reducing agent into the mixture. The final mixture was refluxed at 120 °C for 3 hours with continuous stirring at 250 rpm. After the reaction, the resulting composite was thoroughly washed with DI water to eliminate unreacted substances and by-products. Finally, the washed composite was vacuum-dried at 60 °C for 24 hours to yield the final product.

2.7 Fabrication of the rGO/MnO_2 modified GC electrode

The GC electrode was initially polished to a mirror-like surface using a 0.05 μm alumina slurry on a micro cloth polishing pad. After polishing, the electrode was ultrasonically cleaned in deionized water for 5 minutes to remove residual abrasive particles. For electrode modification, a 1 mg mL^{-1} dispersion of synthesized rGO/MnO_2 was prepared in deionized water using ultrasonication to achieve uniform dispersion. Subsequently, a small aliquot (10 μL) of this suspension was applied onto the polished GC surface by drop-casting and dried at room temperature, forming a uniform coating of active material. The prepared rGO/MnO_2-modified GC electrode was then employed for electrochemical studies.

2.8 Electrochemical experiment

The supercapacitive performance was evaluated by cyclic voltammetry, galvanostatic charging–discharging (GCD), and electrochemical impedance spectroscopy (EIS) measurements

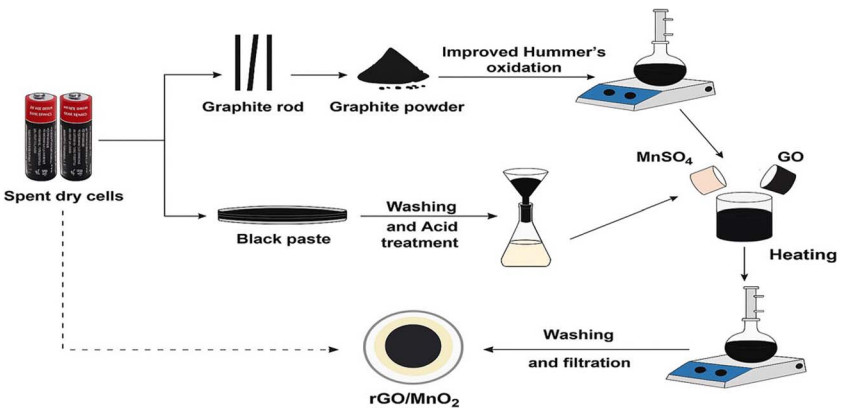

Scheme 1 Schematic illustration of the sustainable synthesis of rGO/MnO_2 nanocomposites from spent dry cells.

using a CHI 660E electrochemical workstation in a three-electrode configuration. The setup consisted of a platinum electrode as the counter, an Ag/AgCl/KCl electrode as the reference, and the rGO/MnO_2 electrode as the working electrode. 1.0 M KOH aqueous solution was used as the electrolyte for conducting all measurements. Eqn (1)–(3) were used to evaluate the electrochemical performance of the electrodes.[32,33]

$$C_{sp} = \frac{It}{M\Delta V} \quad (1)$$

$$E = \frac{C_{sp} \times \Delta V^2}{2 \times 3.6} \quad (2)$$

$$P = \frac{E \times 3600}{t} \quad (3)$$

where, C_{sp} is the specific capacitance (F g^{-1}), I is the constant discharge current (A), M is the active mass of material (g), t is the discharging time (s), and ΔV is the operating potential window (V), E is the energy density (Wh kg^{-1}) and P is the power density (W kg^{-1}).

3 Results and discussion

3.1 Characterization

FTIR was employed to confirm the presence of functional groups in the synthesized materials. Fig. 1(a) compares the FTIR spectra of rGO and rGO/MnO_2. The spectrum of rGO exhibits several distinctive bands. The band at 3439 cm^{-1}, corresponding to O–H stretching, exhibits lower intensity and becomes sharper compared to GO, indicating a significant decrease in hydroxyl groups.[29,34,35] The bands at 2929 cm^{-1} and 2856 cm^{-1} represent the asymmetric and symmetric stretching vibrations of CH_2 groups, respectively.[36] Notably, the absence of the feature at 1734 cm^{-1}, typically assigned to C=O stretching, further confirms the successful reduction of GO.[37,38] The band at 1631 cm^{-1}, corresponding to C=C vibrations, is observed in both spectra, confirming the presence of graphene sheets. Additionally, the bands at 1454 cm^{-1} and 1080 cm^{-1}, corresponding to the stretching vibrations of C–OH and C–O groups, respectively, are characteristic of reduced graphene oxide.[37,39,40] In the FT-IR spectrum of rGO/MnO_2, the bands at 601 and 493 cm^{-1} are attributed to the O–Mn–O and Mn–O stretching modes, respectively, indicating the successful integration of MnO_2 within the rGO matrix.[41] The coexistence of absorption bands corresponding to both rGO and MnO_2 strongly indicates the formation of a composite material. The integration of MnO_2 onto the rGO surface is further confirmed by XRD analysis in addition to morphological and elemental investigations.

Fig. 1(b) presents the XRD patterns of the synthesized rGO and rGO/MnO_2 nanocomposite. The XRD pattern of rGO displays two characteristic features: a broad peak at $2\theta = 24.69°$, associated with the (002) plane, indicative of the disordered graphene layer arrangement, and a second peak at $2\theta = 43.16°$, assigned to the (100) plane of the hexagonal carbon lattice.[42] The removal of oxygen-containing functional groups is evidenced by the decrease in the d-spacing of rGO to 0.361158 nm, compared to the larger spacing of 0.97942 nm reported for graphene oxide (Hidayah *et al.*),[34,35,43] confirming the reduction by hydrazine. The XRD profile of the rGO/MnO_2 nanocomposite exhibits several distinct diffraction peaks at 2θ values of 18.07°, 29.01°, 31.11°, 32.71°, 36.25°, 38.60°, 44.44°, 51.48°, 54.08°, 56.33°, 58.63°, 60.32°, 64.77°, 69.91°, 74.31°, and 78.15°, corresponding to the (200), (101), (110), (020), (103), (211), (004), (220), (204), (105), (312), (303), (321), (224), (040), and (332) planes of MnO_2, respectively.[44–46] The interplanar spacings for the (101), (020), (211), (220), and (321) planes are 0.30, 0.27, 0.23, 0.17, and 0.14 nm, respectively, consistent with standard MnO_2 diffraction data. These diffraction features, combined with FTIR results, validate the successful formation of the rGO/MnO_2 nanocomposite.

The morphologies of rGO and the rGO/MnO_2 composite are presented in Fig. 2. The SEM image of rGO (Fig. 2a) reveals

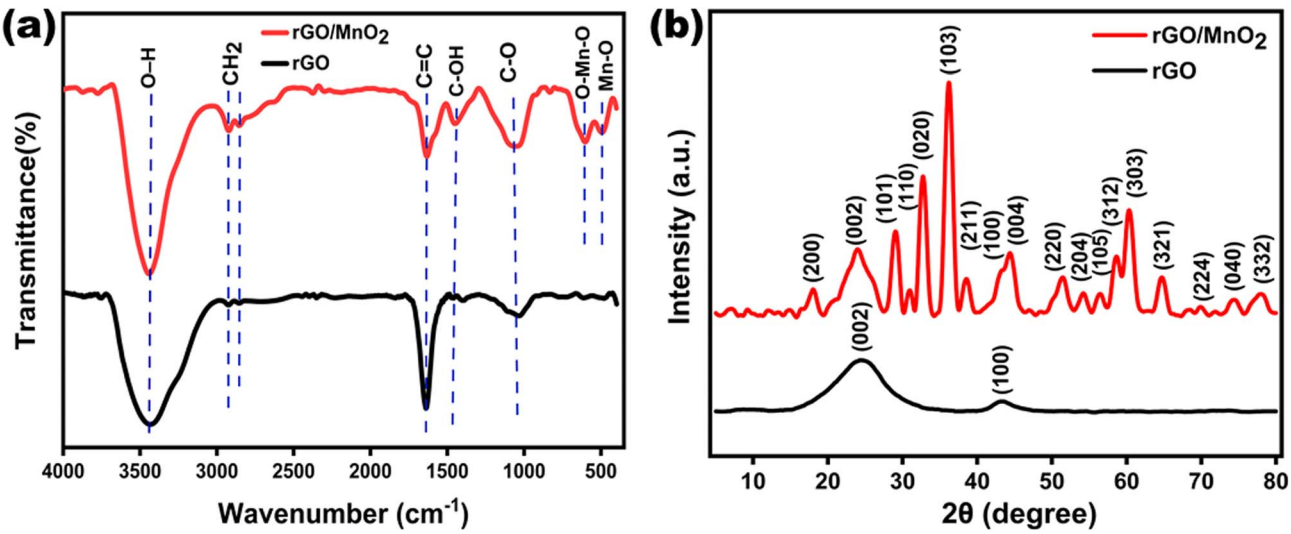

Fig. 1 (a) FTIR spectra of rGO and rGO/MnO_2, (b) XRD pattern of rGO and rGO/MnO_2 nanocomposite.

a thin, sheet-like structure with noticeable crumples and wrinkles on the surface, indicative of a disordered material structure. These surface features increase the available surface area, enhancing ion interaction with the electrolyte.[35,47,48] The SEM images of rGO/MnO_2 in Fig. 2(b and c) illustrate the uniform dispersion of MnO_2 nanoparticles across the rGO sheets. This nanoparticle decoration significantly improves the porosity and accessible surface area of the composite,[49] facilitating better electrolyte penetration and more efficient charge transfer.[50] Fig. 2(d) exhibits the EDX spectrum of the rGO/MnO_2 composite, highlighting its elemental composition. The weight percentage analysis reveals a significant presence of carbon (C) at 62.11%, oxygen (O) at 23.91%, and manganese (Mn) at 13.99%. These results suggest that MnO_2 is effectively integrated into the rGO framework, while the graphene sheets substantially contribute to the overall high carbon content.

TEM analysis of the rGO/MnO_2 composite provides detailed insights into its surface morphology, interlayer spacing, *d*-spacing, particle size, and dispersion, offering a detailed understanding of its nanostructural characteristics. Fig. 3(a–c) presents TEM images of the rGO/MnO_2 composite at various magnifications. These images show a uniform distribution of spherical MnO_2 nanoparticles on the rGO sheets with minimal agglomeration. The well-dispersed nanoparticles form an integrated heterostructure with the graphene matrix that promotes efficient ion and electron transport during charge–discharge cycles.[44] Furthermore, the particle size distribution (Fig. 3(d)) exhibits that the average size of the MnO_2 nanoparticles is approximately 16.01 nm. The HR-TEM microstructure of rGO/MnO_2 (Fig. 3e) reveals a lattice spacing of 0.27 nm, indexed to the (020) plane of MnO_2, which supports the XRD results. The coexistence of rGO sheets and MnO_2 nanoparticles is additionally evidenced by the selected area electron diffraction pattern in Fig. 3(f), which displays amorphous polycrystalline rings with distinct bright spots. The observed diffraction rings correspond to the (020), (220), (321), and (224) planes of MnO_2, as identified in the XRD analysis, confirming the ordered arrangement of MnO_2 nanoparticles within the rGO matrix.[51]

3.2 Electrochemical performances

The cyclic voltammograms (CVs) for rGO, MnO_2, and rGO/MnO_2 modified electrodes were obtained in 1.0 M KOH electrolyte at 50 mV s^{-1} over a potential range of −0.5 to 0.2 V, as shown in Fig. 4(a). The CV shape of the rGO/MnO_2 nanocomposite exhibits a quasi-rectangular shape with distinct redox peaks, demonstrating the coexistence of EDL capacitive behavior and pseudocapacitance.[52,53] The observed redox peaks arise from the intercalation–deintercalation of electrolyte ions within the MnO_2 structure, confirming its pseudocapacitive nature, while the capacitance of rGO was attributed to EDL formation. The pseudocapacitive reactions can be described as eqn (4) and (5)

$$(MnO_2)_{surface} + K^+ + e^- = (MnOOK)_{surface} \quad (4)$$

$$MnO_2 + K^+ + e^- = MnOOK \quad (5)$$

The interconnected network of the rGO/MnO_2 nanocomposite facilitates rapid charge transfer by providing multiple ion-diffusion pathways, while the conductive rGO

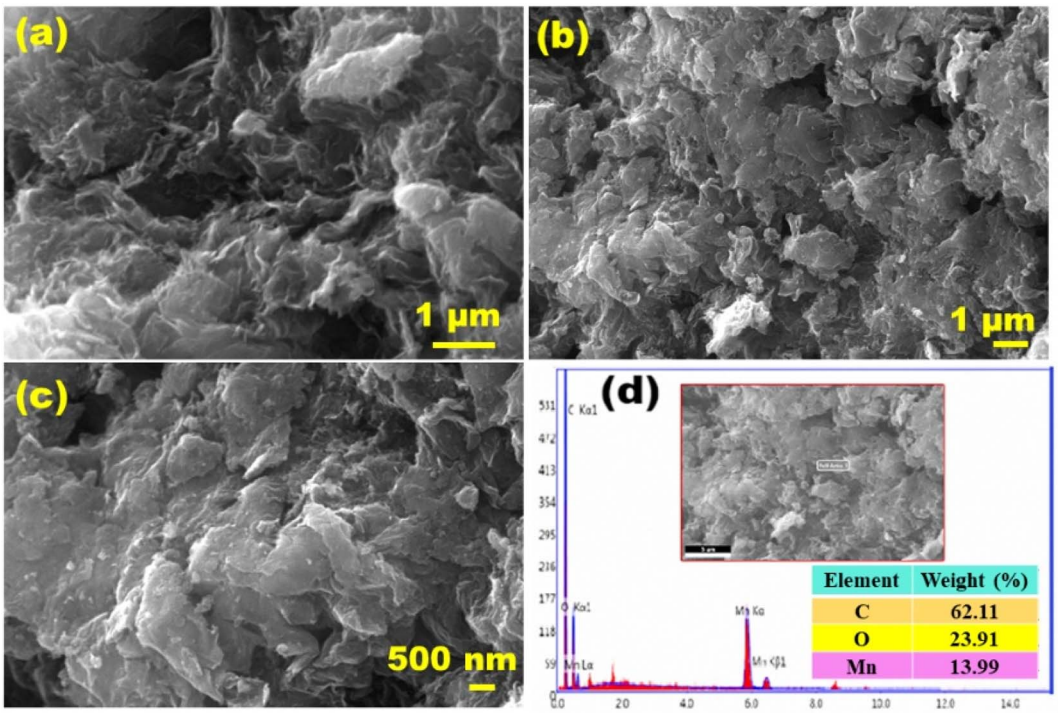

Fig. 2 SEM image of (a) rGO, (b and c) rGO/MnO_2, and (d) EDX spectrum of rGO/MnO_2.

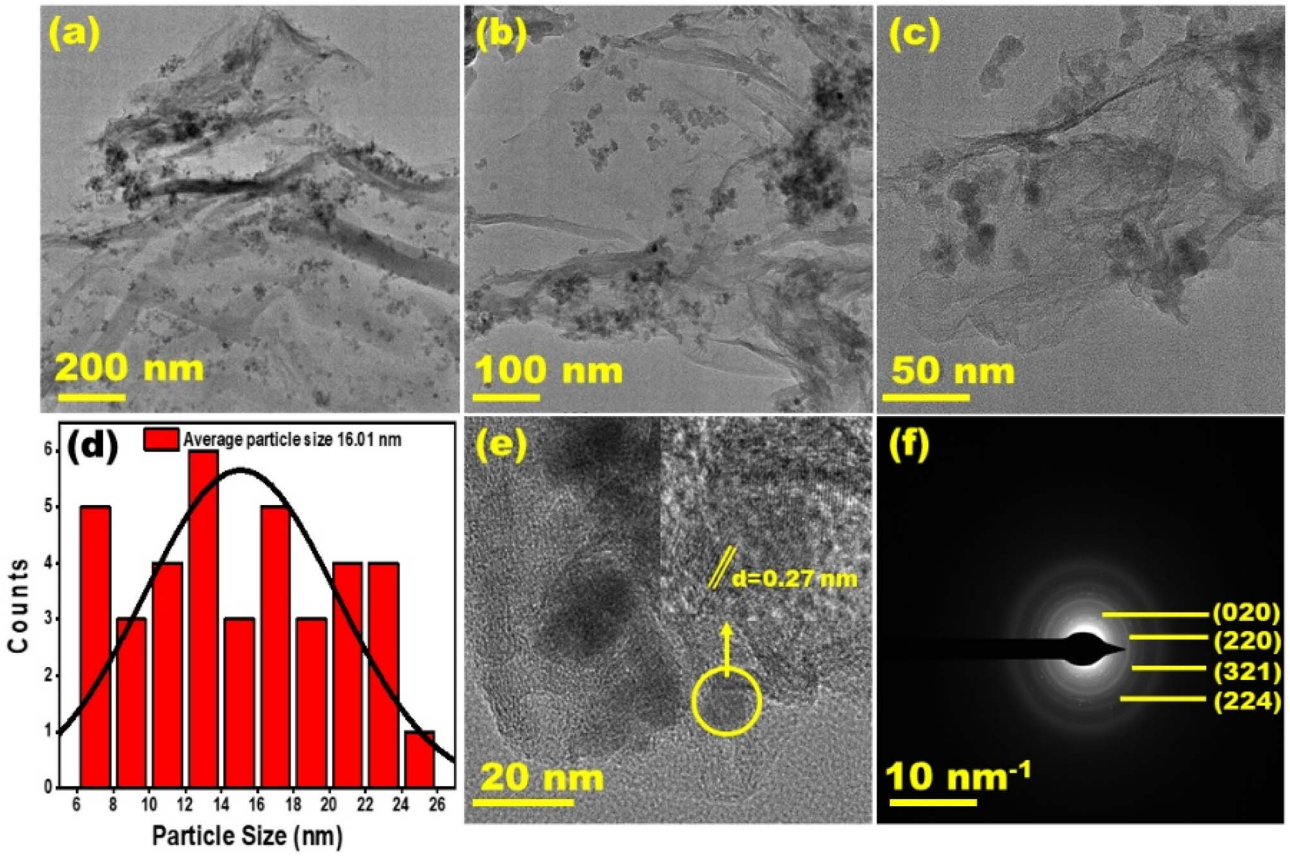

Fig. 3 TEM images of rGO/MnO_2 at (a) 200 nm, (b) 100 nm, (c) 50 nm, (d) particle size distribution, (e) HRTEM image with interplanar spacing, and (f) SAED pattern.

framework enhances electron transport. Simultaneously, MnO_2 nanoparticles offer abundant redox-active sites. As a result, rGO/MnO_2 exhibits a substantially larger CV integrated area compared to individual rGO or MnO_2, demonstrating superior capacitive performance.[44,54] The GCD curves of rGO, MnO_2, and rGO/MnO_2 at 1 A g^{-1} are presented in Fig. 4(b). The non-linear GCD curve of rGO/MnO_2 reflects the dual charge-storage process, wherein rGO contributes through double-layer capacitance and MnO_2 through pseudocapacitive reactions. This observation is in good agreement with the CV results. The rGO/

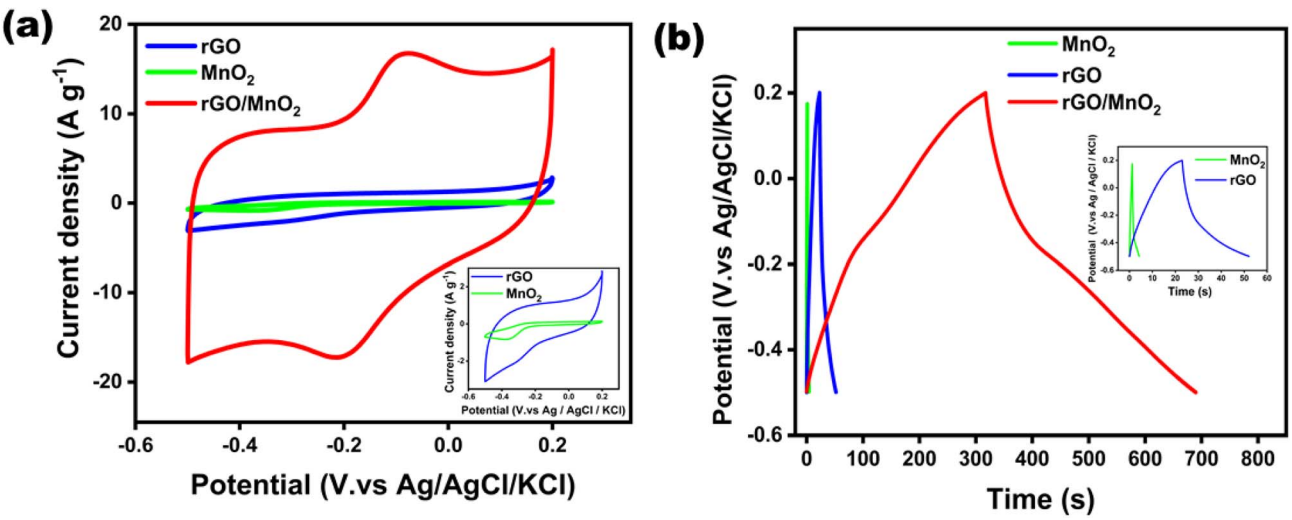

Fig. 4 Electrochemical performance of rGO, MnO_2, and rGO/MnO_2 in 1.0 M KOH. (a) CVs at a scan rate of 50 mV s^{-1} and (b) GCD curves at a current density of 1 A g^{-1}.

Table 1 Comparison of the present work with earlier reported supercapacitor performances[a]

	Electrochemical performance (method: GCD)				
Material	C_{sp} (F g^{-1})	E (Wh kg^{-1})	P (W kg^{-1})	Retention (cycle) (%)	Ref.
DMC/MnO_2	292	34	100	79 (2000)	20
Ni/MnO_2/PC	267.34	28	360	83.6 (5000)	64
NG-MnO_2	220	84.4	396.3	98.3 (1000)	65
rGO-CNTs-MnO_2	332.5	41.6	513.7	89.2 (10 000)	66
rGO/MnO_2	398	—	—	94 (5000)	67
MnO_2/rGO	435	—	—	97.5 (500)	68
MnO_2/Graphene	500	14	250	85.3 (5000)	69
NiO–Mn_2O_3@rGO	420	45	810	91 (500)	70
rGO/MnO_2	532	36.2	350	80 (1500)	This work

[a] PC: porous carbon; NG: nitrogen-doped graphene; CNTs: carbon nanotubes.

MnO_2 electrode achieves a high specific capacitance of 532 F g^{-1} at 1 A g^{-1} (using eqn (1)), substantially outperforming that of individual rGO and MnO_2 electrodes. This enhanced performance arises from the synergistic effect between the conductive rGO framework and the redox-active MnO_2 nanoparticles.[55,56] Notably, this performance is achieved by directly utilizing spent dry cells as the sole source of both graphene oxide and manganese. Compared with conventional systems based on expensive or chemically intensive precursors, this recycling-based strategy offers a sustainable and cost-effective route for fabricating high-performance electrode materials. As summarized in Table 1, the specific capacitance obtained here is comparable to, and in several cases exceeds, previously reported values, highlighting the novelty and competitiveness of this approach.

Moreover, the electrochemical performance of the rGO/MnO_2 composite electrode was further investigated at different scan rates and current densities to evaluate its rate capability. Cyclic voltammetry measurements were conducted at scan rates ranging from 25 to 200 mV s^{-1} (Fig. 5a). The enhancement of current at higher scan rates demonstrates that the rGO/MnO_2 electrode retains its high electrochemical reversibility. The shift of the oxidation peak toward positive potentials and the reduction peak toward negative potentials at higher scan rates is largely attributed to the internal resistance of the electrode.[32] The relationship between specific capacitance and scan rate for the rGO/MnO_2 nanocomposite is presented in Fig. 5(b). The electrode exhibits a specific capacitance of 283.53 F g^{-1} at 25 mV s^{-1} and decreases to 171.97 F g^{-1} at 200 mV s^{-1}. The drop in capacitance at higher scan rates is caused by limited ion mobility into the deeper pores of the electrode, along with an increase in its internal resistance. At higher scan rates, the electrochemical reactions become predominantly surface-limited, leading to a reduction in total charge storage.[57–59] The GCD curves of the rGO/MnO_2 electrode were measured at current densities ranging from 0.5 to 10 A g^{-1} (Fig. 5c). The curves exhibit progressively shorter charge–discharge times as the current density increases, suggesting the presence of kinetic limitations at higher current densities. Correspondingly, the specific capacitance decreases from 721 F g^{-1} at 0.5 A g^{-1} to 280 F g^{-1} at 10 A g^{-1} (Fig. 5d).The decrease is primarily due to incomplete redox reactions and the lower availability of electroactive surface area at higher current densities.[60] Notably, the specific capacitance values obtained from CV differ from those derived from GCD measurements, owing to the fundamental differences in their measurement techniques. CV integrates both electric double-layer and pseudocapacitive contributions during potential sweeps, often resulting in higher capacitance values at low scan rates. In contrast, GCD reflects practical charge–discharge behavior under constant current, which is more influenced by internal resistance and diffusion limitations.[61–63]

Electrochemical impedance spectroscopy was employed to examine the charge transfer processes and electrode–electrolyte interactions in the prepared materials. Fig. 6(a) presents the Nyquist plots of the rGO and the rGO/MnO_2 electrodes in 1.0 M KOH in the frequency ranging from 0.1 Hz to 100 kHz. The Nyquist plot can be divided into two regions: a semicircular feature at high frequency corresponding to charge transfer resistance, and a linear region at low frequency associated with ion diffusion.[57] Fig. 6(b) exhibits the fitted equivalent circuit diagram for better understanding of the electrode behavior, which consists of the solution resistance (R_s), Warburg impedance (W), charge-transfer resistance (R_{ct}), capacitance (C).[44,59,71,72] EIS analysis revealed that the rGO/MnO_2 nanocomposite exhibited a R_s of 9.738 Ω and a remarkably low R_{ct} of 1.512 Ω, indicating excellent electrical conductivity and efficient charge transport at the electrode–electrolyte interface. Additionally, two distinct capacitance components, C_1 (0.006601 F) and C_2 (0.0005494 F), suggest multiple charge storage mechanisms contributing to the enhanced capacitive behavior of the nanocomposite. The energy and power densities of the synthesized rGO/MnO_2 nanocomposite were evaluated using eqn (2) and (3). The nanocomposite delivered a maximum power density of 175 W kg^{-1} at an energy density of 49.06 Wh kg^{-1} at 0.5 Ag^{-1} (Fig. 6(c)), demonstrating its promising electrochemical performance. Furthermore, stability is a key factor for supercapacitors in practical applications. The rGO/MnO_2 electrode retained approximately 80% of its initial specific capacitance after 1500 charge–discharge cycles at

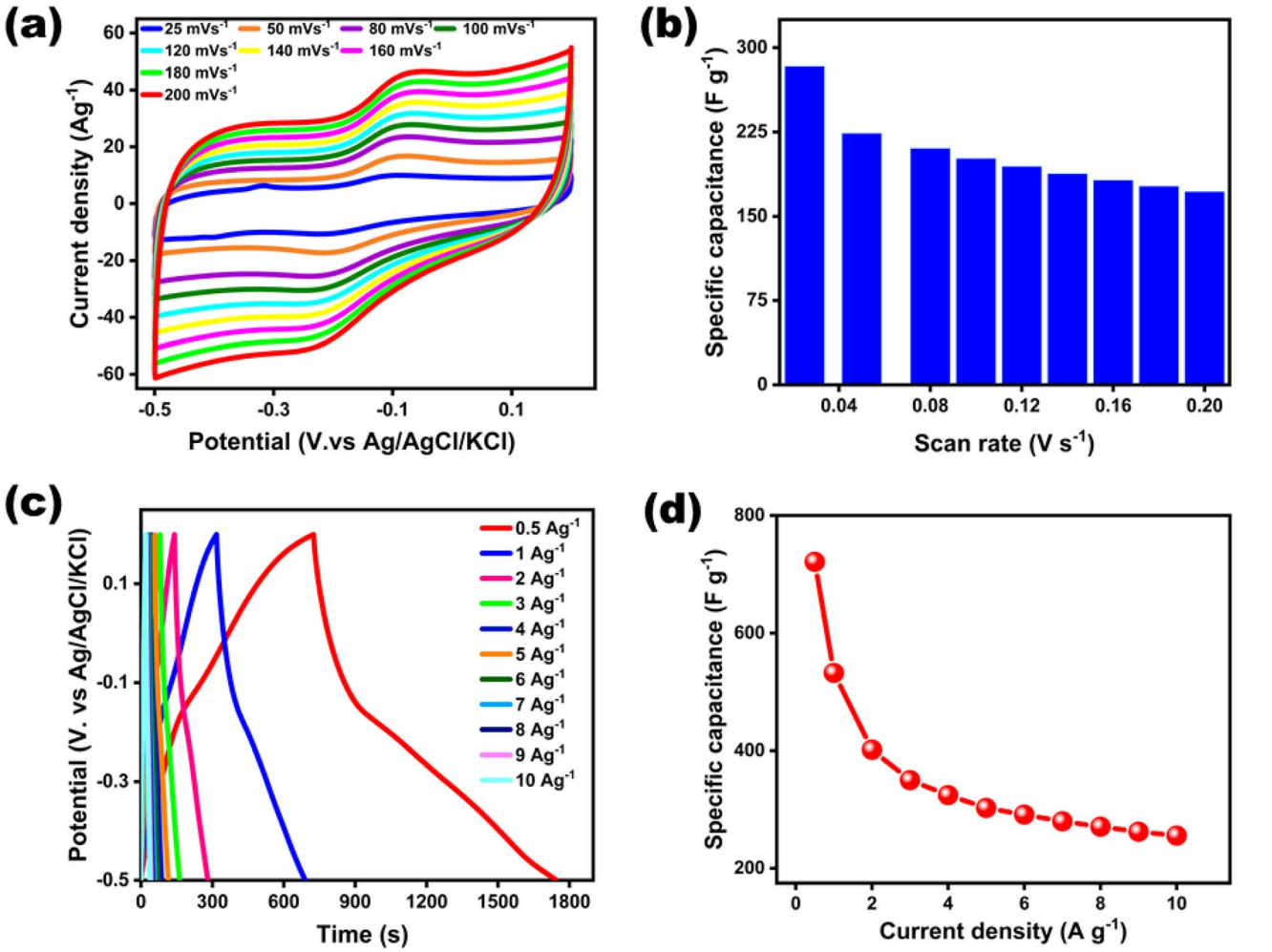

Fig. 5 (a) CVs at various scan rates (25–200 mV s^{-1}), (b) corresponding variation of specific capacitance with scan rate, (c) GCD curves at different current densities (0.5–10 A g^{-1}) and (d) variation of specific capacitance with current density.

100 mV s^{-1}, demonstrating sustained energy storage over extended operation. These results, shown in Fig. 6(d), highlight the electrode's stable performance and its potential for long-term supercapacitor applications.

The electrochemical reversibility of the rGO/MnO_2 electrode was evaluated by plotting the peak current density (i_p) against the square root of the scan rate ($v^{1/2}$) as shown in Fig. 7(a). The linear relationship between current density and $v^{1/2}$ confirms that the electrode exhibits good reversibility. To further elucidate the reaction kinetics and differentiate the charge storage mechanisms, the dependence of the i_p on the v was analyzed using the power-law relationship (eqn (6) and (7))[73]

$$i_p = av^b \quad (6)$$

$$\log i_p = b \log v + \log a \quad (7)$$

where a and b are arbitrary constants related to the electrode material and the charge storage mechanism. Here, the b-value, obtained from the slope of the linear regression of $\log i_p$ *vs.* $\log v$ (Fig. 7b), indicates the dominant charge storage behavior. A b-value of 0.5 signifies a diffusion-controlled process such as faradaic intercalation, whereas a value of 1 denotes surface-controlled capacitive behavior, including both EDLC and pseudocapacitance.[73] The calculated b-value for the anodic process was 0.73, indicating a mixed contribution of both diffusion-controlled and capacitive processes. This hybrid behavior reflects the synergistic charge storage characteristics of the rGO/MnO_2 nanocomposite.[73,74]

Moreover, the relative contributions of capacitive and diffusion-controlled processes were measured using the eqn (8) and (9):[73]

$$i(V) = k_1 v + k_2 v^{1/2} \quad (8)$$

$$i(V)/v^{1/2} = k_1 v^{1/2} + k_2 \quad (9)$$

In eqn (8), the capacitive and diffusive contributions are denoted by $k_1 v$ and $k_2 v^{1/2}$ respectively. The constants k_1 and k_2 are found using eqn (9), which is a rearranged version of eqn (8). The slope (k_1) and intercept (k_2) were determined by linearly fitting the plot $i(V)/v^{1/2}$ *vs.* $v^{1/2}$ at a constant potential (V), as seen

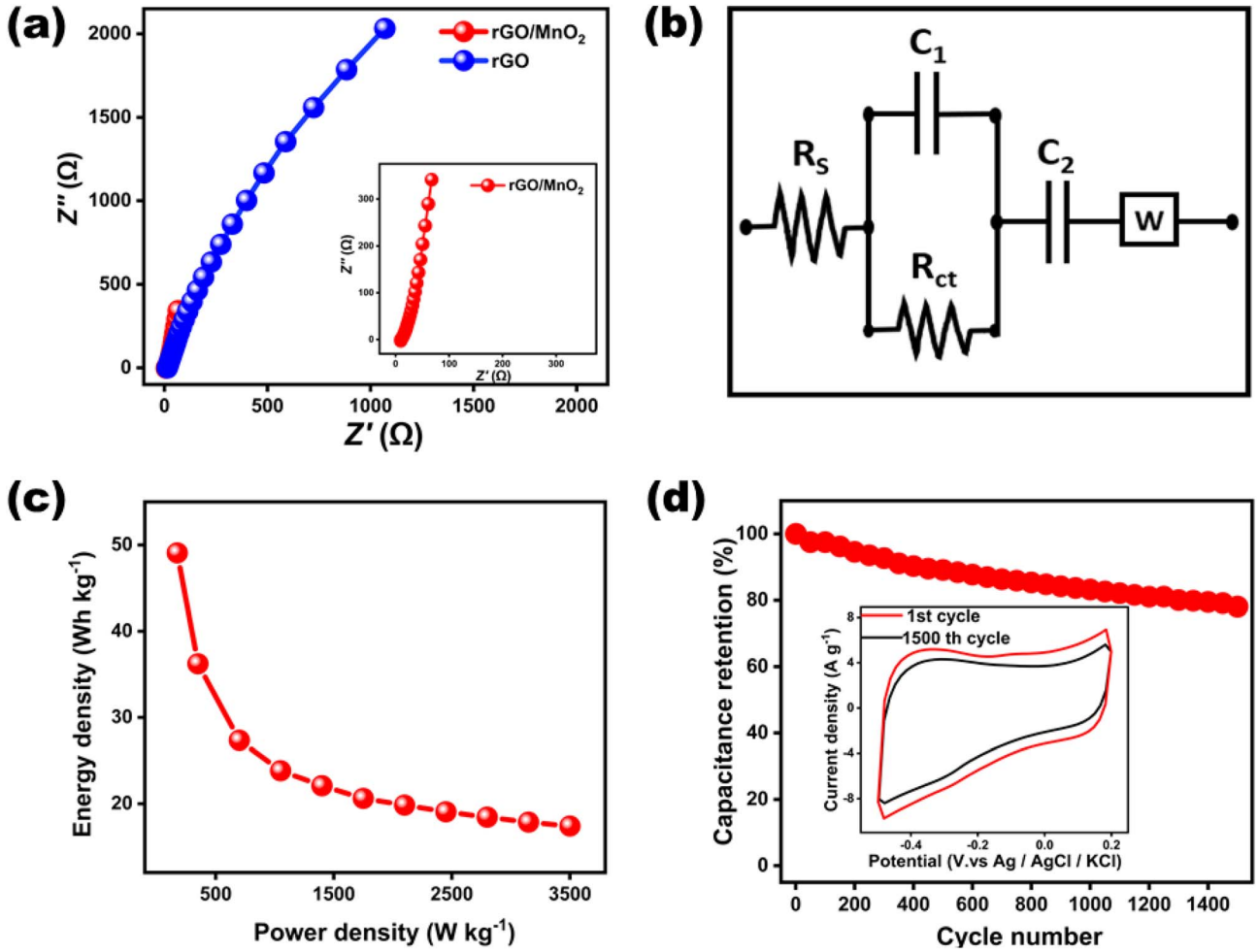

Fig. 6 (a) Nyquist plots of rGO and rGO/MnO_2 measured with a 5 mV signal amplitude, (b) equivalent circuit diagram of rGO/MnO_2, (c) Ragone plot of rGO/MnO_2 (d) cyclic stability of rGO/MnO_2 for 1500 cycles at a scan rate of 100 mV s^{-1}.

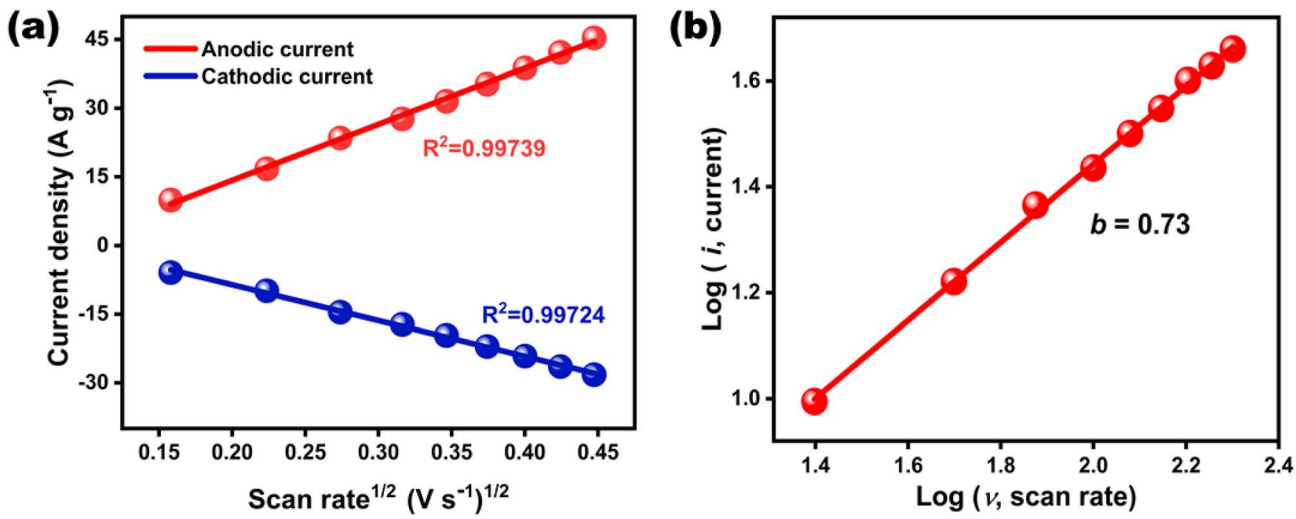

Fig. 7 (a) Cathodic and anodic peak current density (i_p) *vs.* the square root of scan rate ($v^{1/2}$) and (b) plots of log(i_p) and log(v) for rGO/MnO_2.

in Fig. 8(a). The variation in capacitive and diffusive contributions at different scan rates was visualized through a bar graph (Fig. 8b) based on these calculated values of k_1 and k_2.[44,71,73,75] As shown in Fig. 8(b), the capacitive contribution increases from 30.60% at 25 mV s^{-1} to 55.50% at 200 mV s^{-1}. This trend highlights that at higher scan rates, capacitive processes

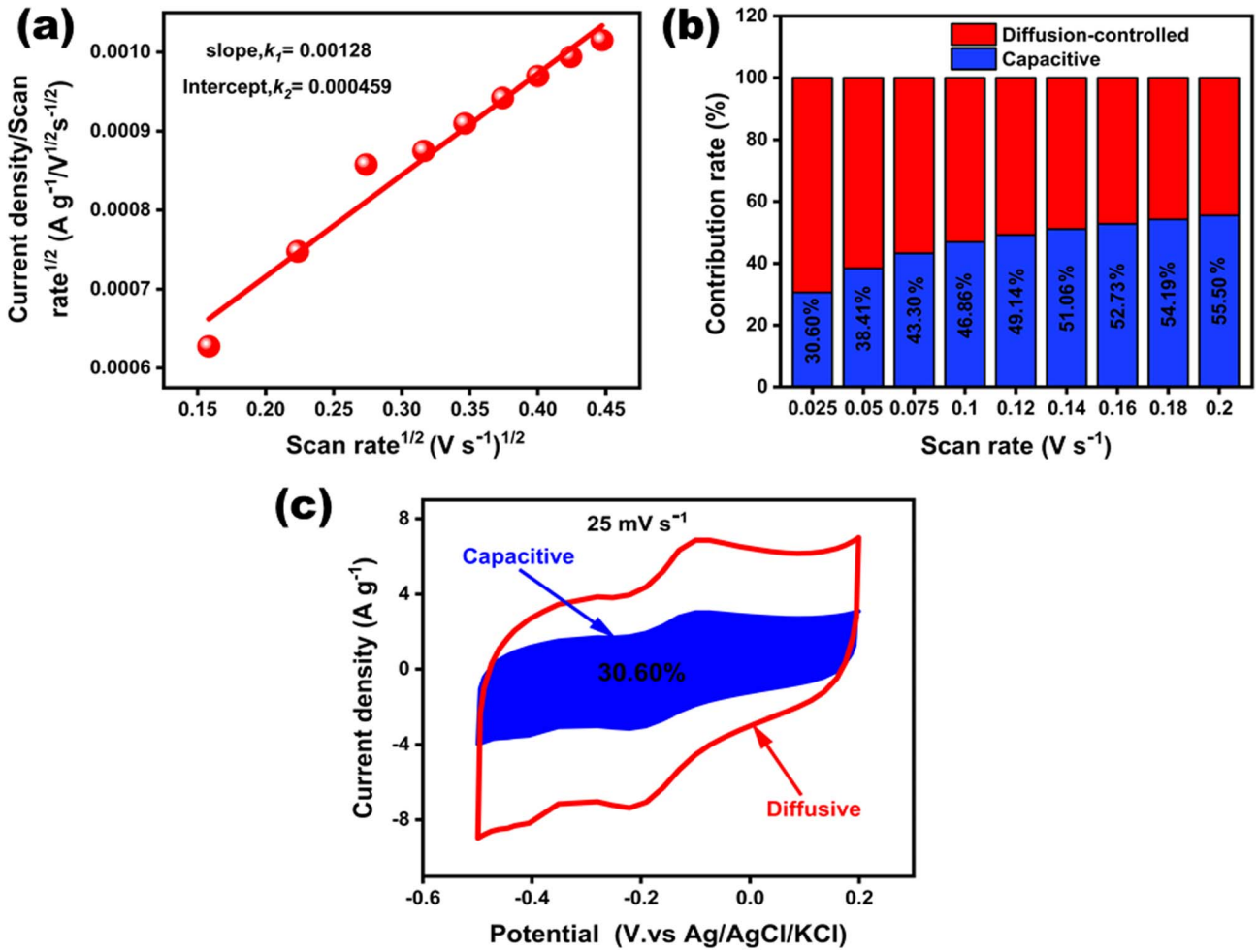

Fig. 8 (a) Plot of $i(V)/v^{1/2}$ *vs.* $v^{1/2}$ for analyzing capacitive and diffusion-controlled charge storage contributions. (b) The capacitive and diffusion-controlled contribution ratios of the rGO/MnO_2 electrode at different scan rate (v), (c) visualization of the capacitive (blue, 30.60%) and diffusion-controlled charge-storage regions for rGO/MnO_2 at 25 mV s^{-1}.

dominate because the limited time restricts ion diffusion and pseudocapacitive intercalation within the electrode structure. Conversely, the diffusion-controlled contribution diminishes with increasing scan rate, consistent with the shorter timescale for electrolyte ion transport.[44,73] Fig. 8(c) further illustrates the deconvolution of capacitive and diffusion-controlled contributions at a representative scan rate of 25 mV s^{-1}. The shaded blue region corresponds to the capacitive component, while the remaining red area denotes the diffusion-controlled contribution. Quantitative analysis indicates that capacitive processes account for 30.60% of the total current at this scan rate, consistent with the lowest value reported in the contribution profile (Fig. 8b). The predominance of the diffusion-controlled region under these conditions highlights the significant role of ion intercalation and redox reactions within the MnO_2 lattice, which remain accessible due to the relatively long timescale for ion transport at lower scan rates. Importantly, the visual separation in Fig. 8(c) underscores that capacitive contributions are distributed across the potential window rather than localized to a specific redox region, reflecting the hybrid charge storage behavior of rGO/MnO_2. This analysis confirms that while diffusion-controlled processes dominate at lower scan rates, capacitive processes progressively contribute more strongly with increasing scan rate, in line with the bar chart trends shown in Fig. 8(b).

4 Conclusions

This work demonstrates a sustainable and effective strategy for fabricating high-performance rGO/MnO_2 composite electrodes using graphene oxide and manganese-based compounds recovered from spent dry cells. The porous and interconnected architecture, confirmed by SEM and TEM, provides abundant active sites and facilitates rapid ion diffusion and charge transfer. As a result, the electrode delivered a high specific capacitance of 532 F g^{-1} at 1 A g^{-1}, along with an energy density of 36.22 Wh kg^{-1} and a power density of 350 W kg^{-1}. Electrochemical impedance spectroscopy further confirmed low internal resistance and favorable ion transport, while cycling tests revealed excellent durability, with 80% capacitance

retention after 1500 CV cycles. By repurposing e-waste into functional electrode materials, this study addresses both environmental sustainability and energy storage challenges. These findings highlight the potential of waste-derived nanocomposites as scalable, eco-friendly alternatives for next-generation supercapacitors. Future efforts will focus on process optimization and device-level integration to advance their practical deployment in green energy technologies.

Author contributions

Othai Saha: formal analysis, data curation, writing original draft. Md Humayun Kabir: conceptualization, supervision, investigation, visualization, funding acquisition, project administration. Md. Mazharul Islam: supervision, investigation, writing – review and editing. Md. Sanwar Hossain: formal analysis, software, writing – review and editing. Muhammad Shahriar Bashar: formal analysis, data analysis. Md Yeasin Pabel: writing – review and editing. Sabina Yasmin: conceptualization, supervision, investigation, visualization, funding acquisition, project administration, writing – review and editing.

Conflicts of interest

There are no conflicts to declare.

Data availability

Data will be made available on request.

Supplementary information is available. See DOI: **https://doi.org/10.1039/d5ra04072h**.

Acknowledgements

The authors gratefully acknowledge the Bangladesh Council of Scientific and Industrial Research (BCSIR) for financial support (R&D ref. no. 39.02.0000.011.14.169.2023/877, dated 17.09.2023). The assistance of IERD, BCSIR, and CARS, Dhaka University, in conducting SEM and XRD analyses is also sincerely appreciated. The authors are also thankful to the Ministry of Science and Technology (MoST), Bangladesh for providing special allocation (ref no. 39.00.0000.009.99.023.23-363-SRG-232372, date: 18/12/2023).

References

1 P. S. N. K, S. Mun Jeong and C. Sekhar Rout, *Energy Adv.*, 2024, **3**, 341–365.
2 S. Veeresh, H. Ganesha, Y. S. Nagaraju, H. Vijeth, M. Vandana, M. Basappa and H. Devendrappa, *J. Energy Storage*, 2022, **52**, 104715.
3 X. Bu, Y. Zhu, C. Wang, W. Li, Y. Xia and Y. Zhao, *ACS Appl. Mater. Interfaces*, 2024, **16**, 7200–7210.
4 J. Yu, X. Sun, X. Shen, D. Zhang, Z. Xie, N. Guo and Y. Wang, *Energy Storage Mater.*, 2025, **76**, 104134.
5 C. Shao, Y. Zhao and L. Qu, *SusMat*, 2022, **2**, 142–160.
6 L. Shen, K. Sun, F. Xi, Z. Jiang, S. Li, Y. Wang, Z. Tong, J. Lu, W. Ma, M. A. Green and X. Hao, *Energy Environ. Sci.*, 2025, **18**, 4348–4361.
7 R. Pal, S. L. Goyal, I. Rawal, A. K. Gupta and J. Ruchi, *Phys. Chem. Solids*, 2021, **154**, 110057.
8 M. A. Rahman, M. A. Haque, M. A. A. Shaikh, C. K. Roy, A. H. Reaz, M. T. A. Shawon, P. K. Baksi, S. Yasmin, M. H. Kabir and S. H. Won, *J. Energy Storage*, 2024, **99**, 113205.
9 H. M. Abuzeid, S. A. Elsherif, N. A. Abdel Ghany and A. M. Hashem, *J. Energy Storage*, 2019, **21**, 156–162.
10 Q. Ke and J. Wang, *J. Materiomics*, 2016, **2**, 37–54.
11 H. T. Das, S. Saravanya and P. Elumalai, *ChemistrySelect*, 2018, **3**, 13275–13283.
12 F. Mojumder, S. Yasmin, M. A. A. Shaikh, P. Chowdhury and M. H. Kabir, *J. Hazard. Mater. Adv.*, 2024, **14**, 100429.
13 S. Yasmin, M. H. Kabir, M. A. A. Shaikh and S. Jeon, *ECS J. Solid State Sci. Technol.*, 2023, **12**, 111004.
14 M. Y. Pabel, M. H. Kabir and S. Yasmin, *J. Energy Storage*, 2025, **119**, 116314.
15 X. Zhang, J. Cai, W. Liu, B. Huang and S. Lin, *J. Appl. Electrochem.*, 2020, **50**, 713–722.
16 J. Yu, M. Li, X. Wang and Z. Yang, *ACS omega*, 2020, **5**(26), 16299–16306.
17 H. Yang, J. Jiang, W. Zhou, L. Lai, L. Xi, Y. M. Lam, Z. Shen, B. Khezri and T. Yu, *Nanoscale Res. Lett.*, 2011, **6**, 531.
18 S. K. Abdel-Aal, S. Y. Attia and S. G. Mohamed, *J. Electron. Mater.*, 2019, **48**, 4977–4986.
19 W. Xu, L. Liu and W. Weng, *Electrochim. Acta*, 2021, **370**, 137713.
20 N. Mohammadi, K. Pourreza, N. Bahrami Adeh and M. Omidvar, *J. Alloys Compd.*, 2021, **883**, 160874.
21 R. Singhal, J. Fagnoni, D. Thorne, P. K. LeMaire, X. Martinez, C. Zhao, R. K. Gupta, D. Uhl, E. Scanley, C. C. Broadbridge, M. Manivannan and R. Pandey, *MRS Adv.*, 2019, **4**, 777–782.
22 S. Goswami, G. R. Dillip, S. Nandy, A. N. Banerjee, A. Pimentel, S. W. Joo, R. Martins and E. Fortunato, *Electrochim. Acta*, 2019, **316**, 202–218.
23 S. Islam, M. H. Kabir, T. Jahan, U. S. Akhtar and S. Yasmin, *Sens. Actuators Phys.*, 2025, **393**, 116791.
24 S. Yasmin, M. G. Azam, M. S. Hossain, U. S. Akhtar and M. H. Kabir, *Heliyon*, 2024, **10**(12), e33317.
25 Md. S. Hossain, S. Yasmin and M. H. Kabir, *J. Saudi Chem. Soc.*, 2024, **28**, 101873.
26 Md. G. Azam, M. H. Kabir, Md. A. A. Shaikh, S. Ahmed, M. Mahmud and S. Yasmin, *J. Water Process Eng.*, 2022, **46**, 102597.
27 B. P. Upoma, S. Yasmin, Md. A. Ali Shaikh, T. Jahan, Md. A. Haque, M. Moniruzzaman and M. H. Kabir, *ACS Omega*, 2022, **7**, 29655–29665.
28 M. Sohag Hossain, M. Humayun Kabir, M. A. A. Shaikh, M. Anamul Haque and S. Yasmin, *RSC Adv.*, 2024, **14**, 1431–1444.
29 Md. Yeasin Pabel, S. Yasmin, M. A. A. Shaikh and M. H. Kabir, *Sens. Actuators Phys.*, 2024, **366**, 115028.

30 S. Yasmin, S. Cho and S. Jeon, *Appl. Surf. Sci.*, 2018, **434**, 905–912.
31 Md. H. Kabir, Md. S. Hossain, M. M. Rahman, Md. Ashrafuzzaman, M. Hasan, Md. Y. Pabel, D. Islam, M. Shahriar Bashar, T. Faruque and S. Yasmin, *ACS Sustain. Resour. Manag.*, 2024, **1**, 1812–1823.
32 M. S. Hossain, M. H. Kabir, M. A. A. Shaikh, M. Y. Pabel and S. Yasmin, *Mater. Chem. Phys.*, 2024, **322**, 129586.
33 Z. Cui, S. Zhan, Y. Luo, Y. Hong, Z. Liu, G. Tang, D. Cai and R. Tong, *Crystals*, 2025, **15**, 346.
34 R. A. Sukumaran, K. Lakavath, V. V. N. P. Kumar, S. Karingula, K. Mahato and Y. Goud Kotagiri, *Nanoscale*, 2025, **17**, 4472–4484.
35 N. M. S. Hidayah, W.-W. Liu, C.-W. Lai, N. Z. Noriman, C.-S. Khe, U. Hashim and H. C. Lee, *AIP Conf. Proc.*, 2017, **1892**, 150002.
36 T. F. Emiru and D. W. Ayele, *Egypt. J. Basic Appl. Sci.*, 2017, **4**, 74–79.
37 Facile One-Pot Preparation of Silver/Reduced Graphene Oxide Nanoc: Ingenta Connect, **https://www.ingentaconnect.com/contentone/asp/jnn/2016/00000016/00000007/art00061**, accessed 17 March 2025.
38 M. Humayun Kabir, M. Yeasin Pabel, N. Tasnim Bristy, M. Abdus Salam, M. Shahriar Bashar and S. Yasmin, *RSC Adv.*, 2024, **14**, 36073–36083.
39 S. K. Abdel-Aal, S. Y. Attia and S. G. Mohamed, *J. Electron. Mater.*, 2019, **48**, 4977–4986.
40 T. S. Munonde, A. Nqombolo, S. Hobongwana, A. Mpupa and P. N. Nomngongo, *Heliyon*, 2023, **9**(4), e15502.
41 Y. Dessie, S. Tadesse, R. Eswaramoorthy and Y. Adimasu, *Life*, 2021, **14**, 541–568.
42 N. T. Dipannita, S. Yasmin, M. K. Hasan, M. S. Hossain, M. A. Somapti and M. H. Kabir, *RSC Adv.*, 2025, **15**, 35219–35232.
43 I. Boukhoubza, M. Khenfouch, M. Achehboune, B. M. Mothudi, I. Zorkani and A. Jorio, *J. Phys.: Conf. Ser.*, 2019, **1292**, 012011.
44 D. Jhankal, M. Saquib Khan, P. Shakya, N. Bhardwaj, B. Yadav, K. K. Jhankal and K. Sachdev, *Energy Adv.*, 2024, **3**, 191–202.
45 B. Usharani and V. Manivannan, *Mater. Lett. X*, 2022, **15**, 100162.
46 A. Kumar, M. S. Aathira, U. Pal and S. L. Jain, *ChemCatChem*, 2018, **10**, 1844–1852.
47 S. Yasmin, Y. Joo and S. Jeon, *Appl. Surf. Sci.*, 2017, **406**, 226–234.
48 D. Govindarajan, V. Uma Shankar and R. Gopalakrishnan, *J. Mater. Sci. Mater. Electron.*, 2019, **30**, 16142–16155.
49 N. H. Khand, A. R. Solangi, H. Shaikh, Z.-H. Shah, S. Bhagat, S. T. H. Sherazi and E. A. López-Maldonado, *Microchim. Acta*, 2024, **191**, 342.
50 D. A. Bograchev, Y. M. Volfkovich, V. E. Sosenkin, O. A. Podgornova and N. V. Kosova, *Energies*, 2020, **13**, 542.
51 MnO_2@Reduced Graphene Oxide Nanocomposite-Based Electrochemical Sensor for the Simultaneous Determination of Trace Cd(II), Zn(II) and Cu(II) in Water Samples, **https://www.mdpi.com/2077-0375/11/7/517**, accessed 24 March 2025.
52 A. Gangwar, T. Das, S. K. Shaw and N. K. Prasad, *Electrochim. Acta*, 2021, **390**, 138823.
53 M. Manikandan, P. N. Francis, S. Dhanuskodi, N. Maheswari and G. Muralidharan, *J. Mater. Sci. Mater. Electron.*, 2018, **29**, 17397–17404.
54 J. Samdani, K. Samdani, N. H. Kim and J. H. Lee, *Appl. Surf. Sci.*, 2017, **399**, 95–105.
55 S. R. Charandabinezhad, H. Asgharzadeh and N. Arsalani, *J. Mater. Sci. Mater. Electron.*, 2021, **32**, 1864–1876.
56 B. S. Singu and K. R. Yoon, *J. Alloys Compd.*, 2019, **770**, 1189–1199.
57 S. R. Charandabinezhad, H. Asgharzadeh and N. Arsalani, *J. Mater. Sci. Mater. Electron.*, 2021, **32**, 1864–1876.
58 Z. Çıplak, *J. Electron. Mater.*, 2022, **51**, 1077–1088.
59 G. S. Gund, D. P. Dubal, B. H. Patil, S. S. Shinde and C. D. Lokhande, *Electrochim. Acta*, 2013, **92**, 205–215.
60 J. Dong, G. Lu, F. Wu, C. Xu, X. Kang and Z. Cheng, *Appl. Surf. Sci.*, 2018, **427**, 986–993.
61 J. P. dos Santos, F. Rufino, J. Ota, R. Fernandes, R. Vicentini, C. Pagan, L. Da Silva and H. Zanin, *J. Energy Chem.*, 2023, **80**, 265–283.
62 M. A. A. M. Abid, M. I. Radzi, M. Mupit, H. Osman, R. F. Munawar, K. F. Samat, M. S. M. Suan, K. Isomura and M. R. Islam, *Malays. J. Compos. Sci. Manuf.*, 2020, **3**, 14–26.
63 Y. Zhang, L. Gao, M. Cao and S. Li, *Materials*, 2024, **17**, 3516.
64 X. Ji, D. Sun, W. Zou, Z. Wang and D. Sun, *J. Alloys Compd.*, 2021, **876**, 160112.
65 J. Dong, G. Lu, F. Wu, C. Xu, X. Kang and Z. Cheng, *Appl. Surf. Sci.*, 2018, **427**, 986–993.
66 C. Tang, K. Zhao, Y. Tang, F. Li and Q. Meng, *Electrochim. Acta*, 2021, **375**, 137960.
67 J. Salamon, A. Simi, H. J. Prabu, A. F. Sahayaraj, A. J. S. Kennedy, J. Beny, V. Snowlin, R. R. Gopi, I. Johnson and A. Fatehmulla, *J. Electron. Mater.*, 2025, **54**, 510–522.
68 D. N. Kang, J. Li, Y. H. Xu and W. X. Huang, *Int. J. Electrochem. Sci.*, 2020, **15**, 6091–6108.
69 X. Liu, B. Liang, X. Hong and J. Long, *Front. Chem.*, 2022, **10**, 870541.
70 D. Bejjanki and S. K. Puttapati, *J. Electron. Mater.*, 2023, **52**, 4729–4737.
71 S. Liang, H. Wang, Y. Li, H. Qin, Z. Luo and L. Chen, *Appl. Surf. Sci.*, 2021, **567**, 150809.
72 α-Manganese Dioxide (α-MnO_2) Coated with Polyaniline (PANI) and Reduced Graphene Oxide (rGO)-Based Nanocomposite for Supercapacitor Application, **https://www.mdpi.com/2504-477X/7/4/167**, accessed 10 April 2025.
73 Md. A. Hasan and Md. M. Islam, *J. Energy Storage*, 2024, **98**, 113015.
74 K. Wu, X. Li, Z. Zhu, G. Ma, Y. Ding, J. Wang, Z. Ye, X. Peng, D. Li and Z. Jin, *J. Mater. Sci.: Mater. Electron.*, 2022, **33**, 13326–13338.
75 Z. Fan, J. Ren, F. Zhang, T. Gu, S. Zhang, R.-P. Ren and Y.-K. Lv, *J. Mater. Sci.*, 2022, **57**, 1281–1290.